Supporting Information for

Trends and Interannual Variability in the Dissolved Inorganic Carbon Pool

S1: Domain

We demonstrate the horizontal domain of MOBO-DIC (this study) in Fig. S1, highlighting that compared to the monthly climatology of MOBO-DIC (Keppler et al., 2020), the domain has increased due to an increase in the domain of the Argo-based temperature and salinity fields we use as predictors (Roemmich & Gilson, 2009). While the monthly climatology of MOBO-DIC extended from 65° N to 65° S, MOBO-DIC extends up to 80° N in the Atlantic. Additionally, some coastal zones that were previously masked are now included.

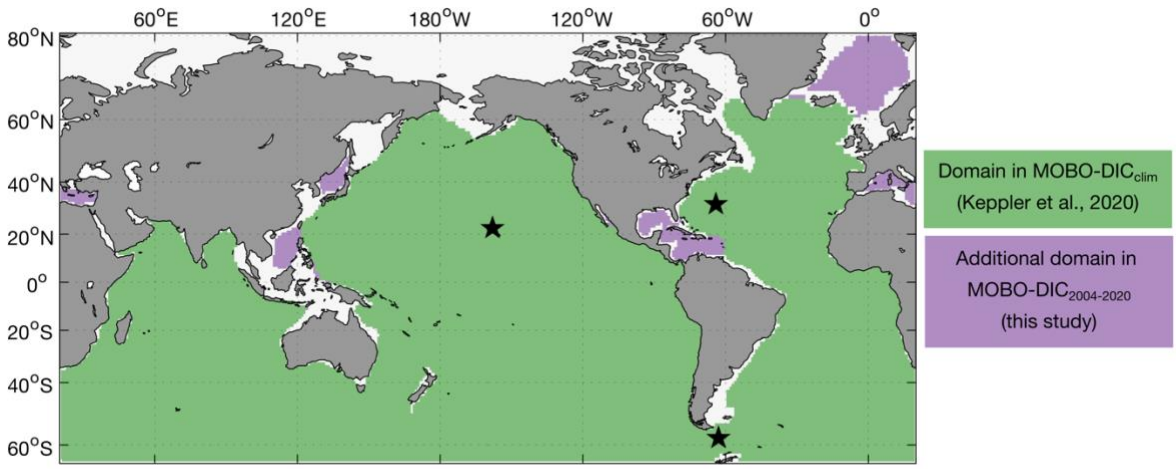

Figure S1: Horizontal domain of MOBO-DIC. Green areas illustrate the domain in the monthly climatology of MOBO-DIC, while the purple regions illustrate the additional regions in MOBO-DIC (this study). Black stars mark the location of the BATS, HOT, and Drake Passage time-series stations (from north to south), which are discussed in Section S5.2.

S2: Clusters

We apply an ensemble approach, where we create an ensemble of SOM-clusters to avoid boundary problems, following Gregor & Gruber (2021). Fig. S2 illustrates first the shape of the clusters and then demonstrates that the clusters are most variable around the boundaries.

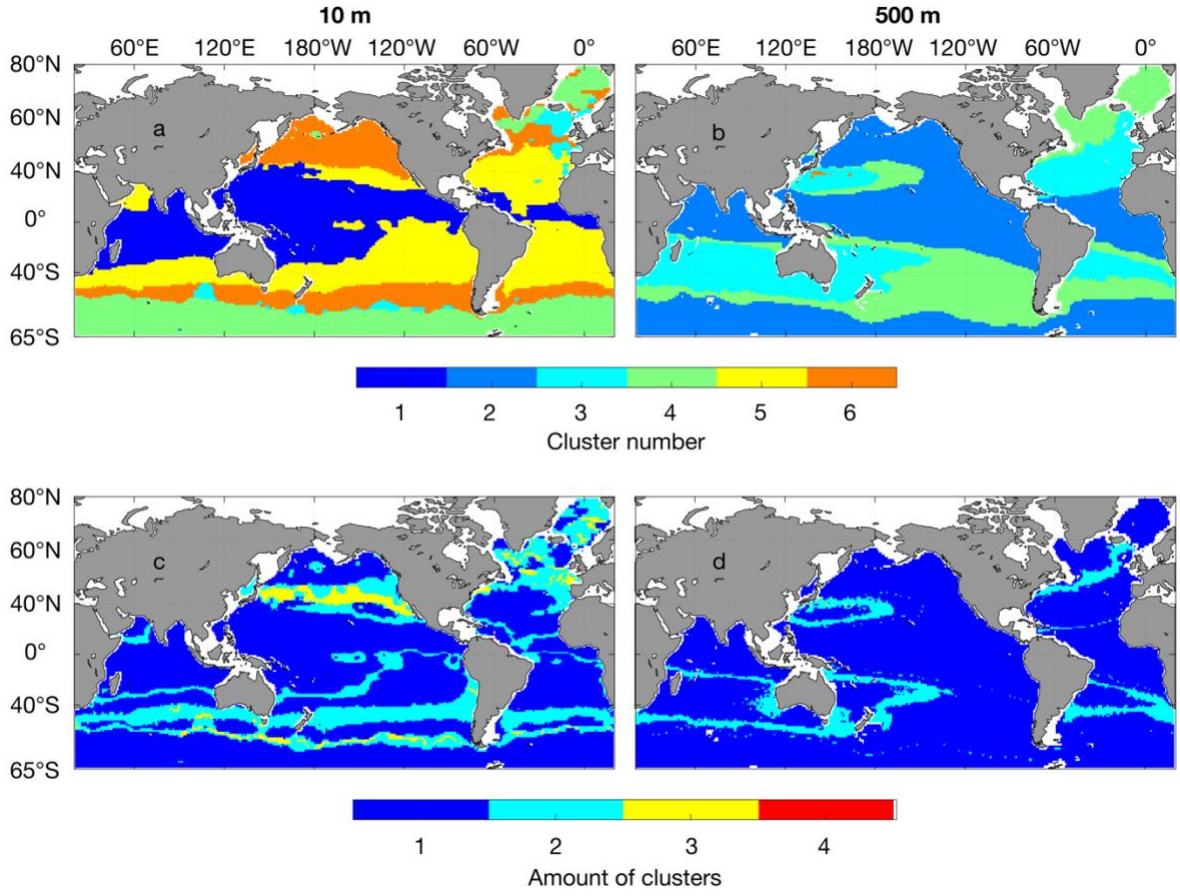

Figure S2. Shape and variability of the clusters. Maps of the clusters in January 2004 on 2 depth levels (a,b), and the number of different clusters at the same depth levels (c,d) at 10 m (a,c) and 500 m (b,d).

S3: Global upscaling of the inventory changes

After calculating the change in the integrated trend i.e., the inventory change in our study domain, we conduct an upscaling to estimate the global changes in the salinity-normalized DIC (sDIC) that includes regions beyond our domain, i.e., the high latitudes, coastal regions, and below 1500 m. For the high latitudes and coastal regions that are masked in MOBO-DIC, we take the global mean trend of MOBO-DIC at each depth level and assume the masked grid cells have the same trend at these depth levels and calculate the vertical integral in these regions. As the trend in sDIC decreases with depth in the upper 1500 m, we assume that the trend below 1500 m continues to weaken with depth and propose that between 1500 m and 4000 m the trend should be between 0 and the trend at 1500 m. We thus calculate the vertical integral between 1500 m and 4000 m, using the trend at each latitude-longitude grid cell at 1500 m in the remaining water column. We add half of that amount to our estimate and add the remaining half to the uncertainty to our global upscaled estimate. As discussed further below, our estimate of the sDIC trend between 1500 m and 4000 m yields 6±6 Pg C during our study period, i.e., 0.4±0.4 Pg C yr^{-1}. This estimate is higher than the increase in C_{ant} between 1994 and 2007 in the same depth range, which amounts to approximately 3±0.4 Pg C, i.e., 0.2±0.0 Pg C yr^{-1}. In the assumption that most of the long-term changes are anthropogenic, our estimate of the positive trend in DIC between 1500 m and 4000 m might be overestimated, but within the uncertainties. To obtain the depth until where we vertically integrate, we use the bathymetry from Etopo2 (2001). Previous studies have found that there is no significant increase in C_{ant} below 4000 m (Gruber et al., 2019). It is possible that there are changes in the natural carbon (C_{nat}) below 4000 m, however, we are unable to quantify this contribution here. As the trend in sDIC decreases with depth in the upper 1500 m, we assume no significant trend in the total sDIC below 4000 m.

S4: Uncertainties

The prediction uncertainty, which we define as the uncertainty linked to our method, is highlighted in Fig. S3. This uncertainty is estimated as the standard deviation across the 15-member ensemble from our bootstrapping approach. Note that the overall uncertainty of our product is, however, higher than the prediction uncertainty as described in Eq. 1 of the Main Text. In addition, Fig. S3 illustrates the temporal mean of the prediction uncertainty. At a single point in time, the prediction uncertainty may differ from this mean.

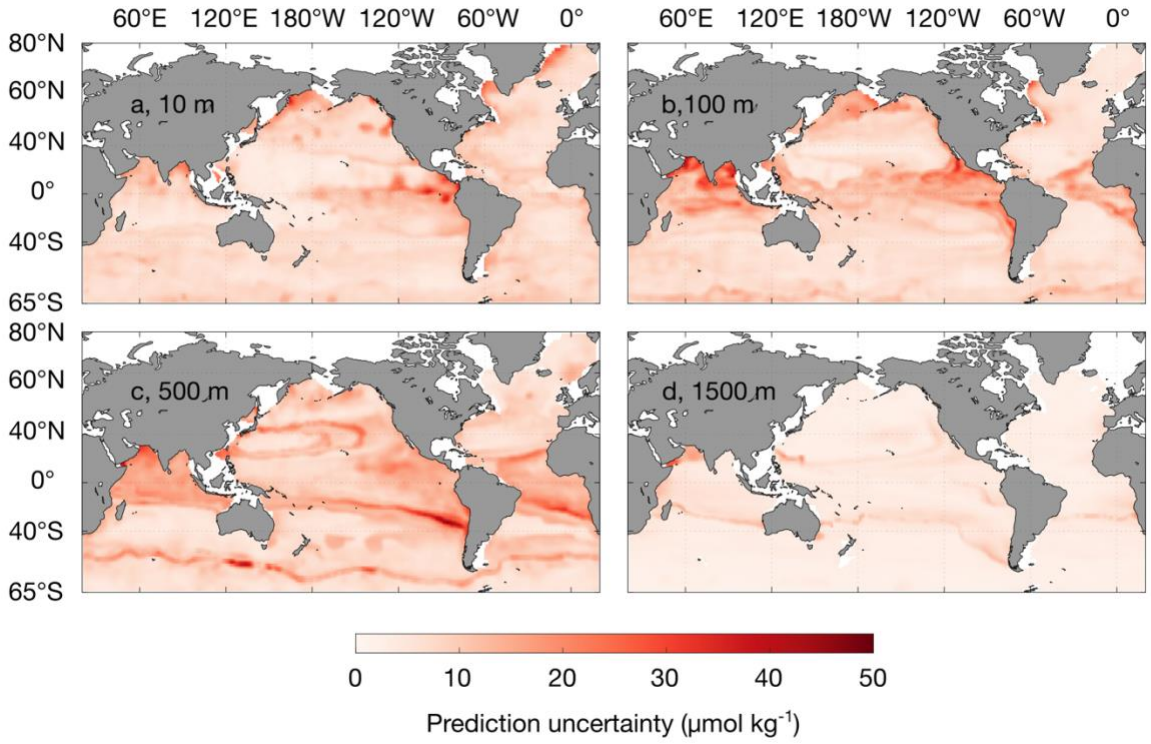

Figure S3. Maps of the prediction uncertainty of MOBO-DIC on four depth levels: (a) 10, (b) 100, (c) 500, and (d) 1500 m.

S5: Comparison with the state of the art

S5.1: Residuals from the GLODAP data

Unlike an interpolation, our mapping method estimates the target data at all grid points, while minimizing the difference between the target data (i.e., GLODAPv2.2021) and the mapped estimate (i.e., MOBO-DIC). Thus, there is a difference between the GLODAP data and MOBO-DIC. Here, we present these residuals to get a better handle on the quality of our fits (Fig. S4). We calculate the residuals by subtracting the GLODAP data at each point in time and space from our MOBO-DIC estimate. In the maps below we display the temporal mean of these residuals on different depth levels. While some regions have a positive bias, others have a negative one, leading to a global mean bias of 0. The same regions can show different residuals at different depths and there is also no indication of certain depth levels being more prone to over- or underestimate. The global mean root mean square difference (RMSD) between GLODAP and MOBO-DIC is 16 µmol kg^{-1}.

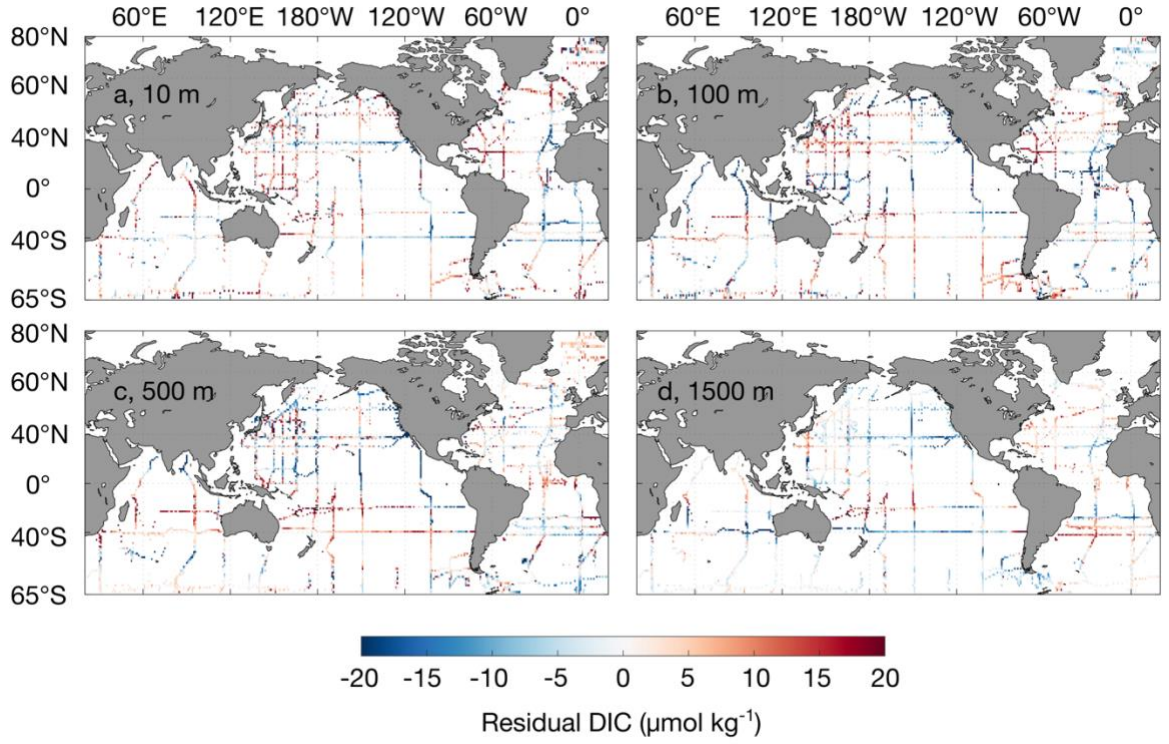

Figure S4. Maps of the temporal mean residuals (MOBO-DIC – GLODAP) at (a) 10, (b) 100, (c) 500, and (d) 1500 m.

S5.2 Climatologies (Lauvset, Broullón, climatology of MOBO-DIC)

The current state-of-the art climatology of global-scale DIC was created by Lauvset et al. (2016), who optimally interpolated GLODAPv2 ship data to create an annual-mean climatology of DIC in the upper 5500 m of the ocean. Recently, Broullón et al. (2020) and Keppler et al. (2020) used machine learning approaches to create monthly climatologies of DIC, the first global-scale time-varying DIC fields in the upper ocean. Although the climatologies cannot be used to assess the interannual variability of MOBO-DIC, we use these data sets to assess the differences in the temporal mean distribution (Lauvset et al., 2016), and the seasonal cycles (Broullón et al., 2020; Keppler et al., 2020) as a first order test of our method in comparison to the state of the art at lower temporal resolution.

In the upper ~200 m, MOBO-DIC tends to yield higher DIC concentrations than the Lauvset-climatology (differences up to ~50 µmol kg^{-1}), except for the northern Indian Ocean, which has lower values in the upper ~600 m (Fig. S5). Below ~200 m, the differences between the two products are smaller and both positive and negative. Similar differences were observed when comparing climatology of MOBO-DIC (Keppler et al., 2020) with the Lauvset climatology (Supporting Information of Keppler et al., 2020). The higher surface concentrations in both MOBO-DIC_{clim} and MOBO-DIC can be largely attributed to the fact that MOBO-DIC covers a later period (2004-2018 and 2004-2020, for the climatology and this study, respectively) than the Lauvset climatology, which is normalized to the year 2002. We expect other differences between the two products to be due to different data used (i.e., Lauvset use data from before 2004), as well as difference in the mapping method. This is further discussed in the Supporting Information of Keppler et al. (2020).

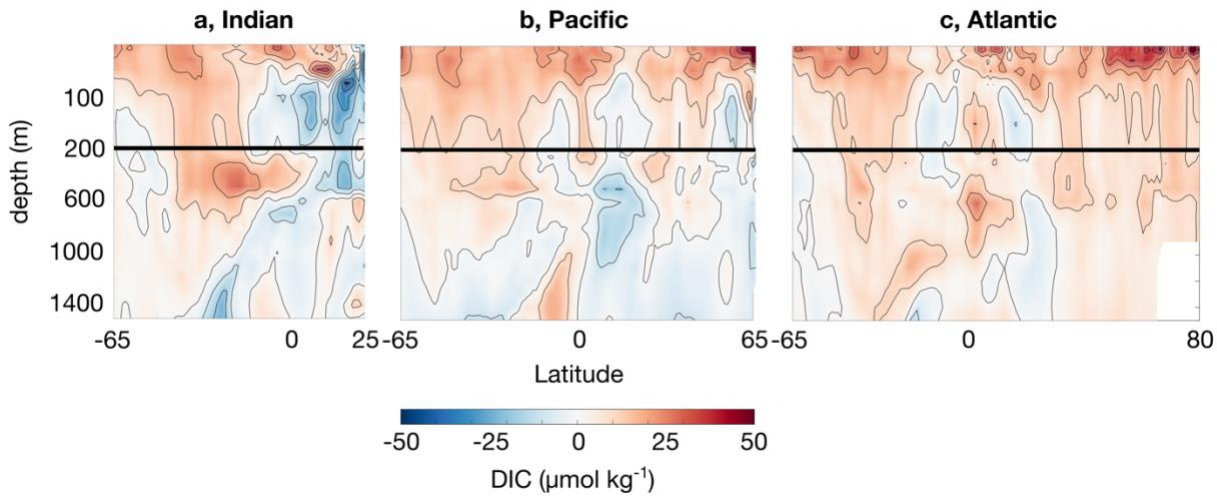

Figure S5: Zonal mean difference between the mean DIC in the climatology by Lauvset et al. (2016) and MOBO-DIC (MOBO-DIC - Lauvset) as a function of latitude (x-axis) and depth (y-axis), in the Indian (a), Pacific (b), and Atlantic Ocean (c). Zoomed into the upper 200 m.

The comparison of the seasonal cycle of DIC with the existing monthly climatologies is encouraging: the three products agree on the distribution and magnitude of the amplitude and phase (Fig. S6). In all products, the largest surface amplitudes are in the north Pacific (more than 50 µmol kg^{-1}), while the Labrador Sea, equatorial East Pacific and equatorial East Atlantic also have elevated surface amplitudes (Fig. S6 a-c). The seasonal maxima tend to be in hemispheric winter, due to deeper mixed layers in winter. The magnitude of the seasonal cycle tends to be weakest near the equator and largest near the poles due to the strength in seasonal forcing. The processes behind these patterns are described in more detail Keppler et al. (2020).

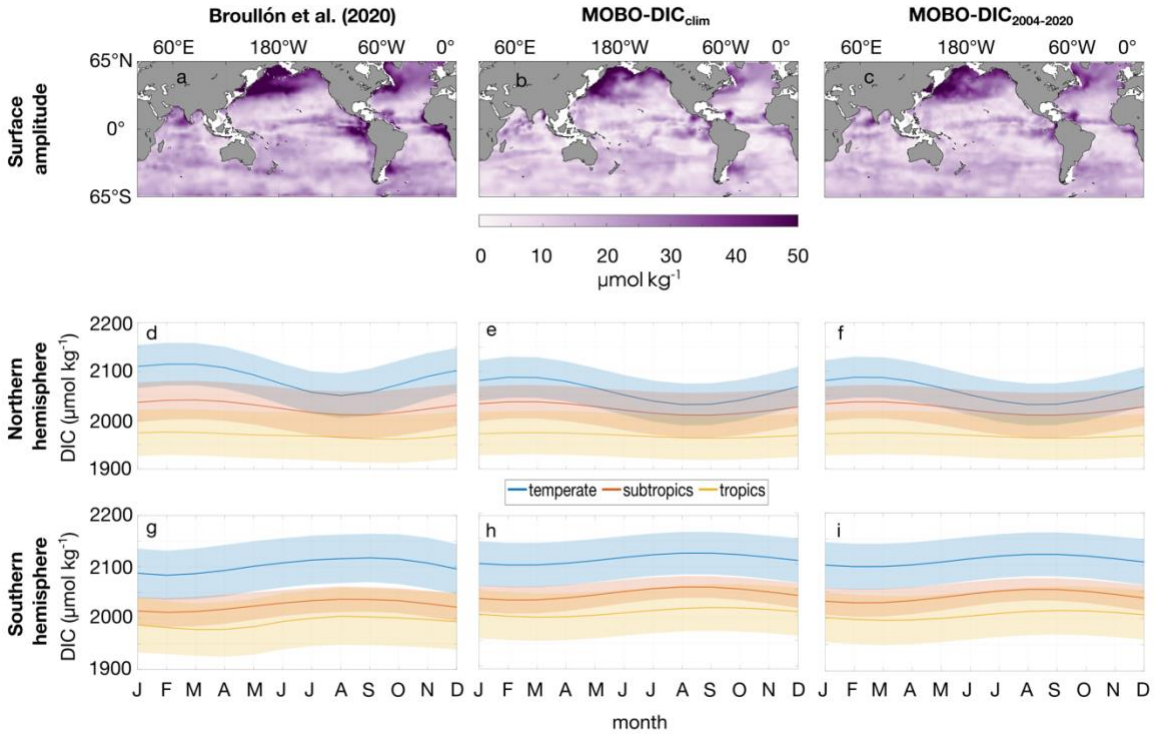

Figure S6: Amplitude of the seasonal cycle of DIC at 2.5 m in the monthly climatology by Broullón et al. (2020) (a), climatology of MOBO-DIC (b), and MOBO-DIC (c). The mean seasonal cycle in climatic zones in the northern (d-f) and southern hemisphere (g-i) for the same three datasets (Broullón et al. (2020) (d,g), climatology of MOBO-DIC (e,h), and MOBO-DIC (f,i). Temperate is from 35° to 65°, subtropics from 23° to 35°, tropics from 0° to 23°, for each hemisphere. Shading illustrates the standard deviation in the latitude-longitude space.

S6: Comparison with independent data

S6.1 Comparison with synthetic data (HAMOCC)

To date, there is no estimate of monthly inter-annually varying mapped fields of interior DIC at a global scale. We therefore conduct an assessment with synthetic data from the ocean biogeochemical model HAMOCC (Ilyina et al., 2013; Mauritsen et al., 2019). Here, we subsample the full model field of sDIC in the HAMOCC model at the time and location where we have observations of DIC in GLODAPv2.2021, and then run our cluster-regression method to recreate the full model field of sDIC. We then compare our sDIC reconstruction in HAMOCC with the actual sDIC in HAMOCC at every grid cell. Please refer to Keppler et al. (2020) and its Supporting Information for a more detailed description of this method with synthetic data.

The trend in sDIC in HAMOCC and our MOBO-DIC reconstruction of HAMOCC display very comparable spatial patterns (Fig. S7). There are both regions of under estimation and over estimation of the trend, indicating that there is no systematic bias in our method. When comparing the depth-integrated change in sDIC, we find again that in most regions, the spatial distributions agree well. However, in the eastern tropical Pacific, the trend is higher in our MOBO-DIC reconstruction of HAMOCC, than in HAMOCC. This difference mostly comes from the deep ocean between 1000 and 1500 m, where we find strong positive trends, that seem to be artifactual, possibly due to overfitting in our estimate with synthetic data (Fig. S7i). However, our estimate with real observations does not have these large positive trends at depth (see Fig. 1 in the Main Text), indicating that this is only a feature in our estimate with synthetic data. Integrated over the whole domain, the total increase in sDIC in the upper 1500 m is 1.7 Pg C yr^{-1} in the HAMOCC model, and 1.9 Pg C yr^{-1} in our MOBO-DIC reconstruction of HAMOCC. The larger increase in our MOBO-DIC reconstruction of HAMOCC is mostly due to the artifact at depth accumulating in the vertical integration.

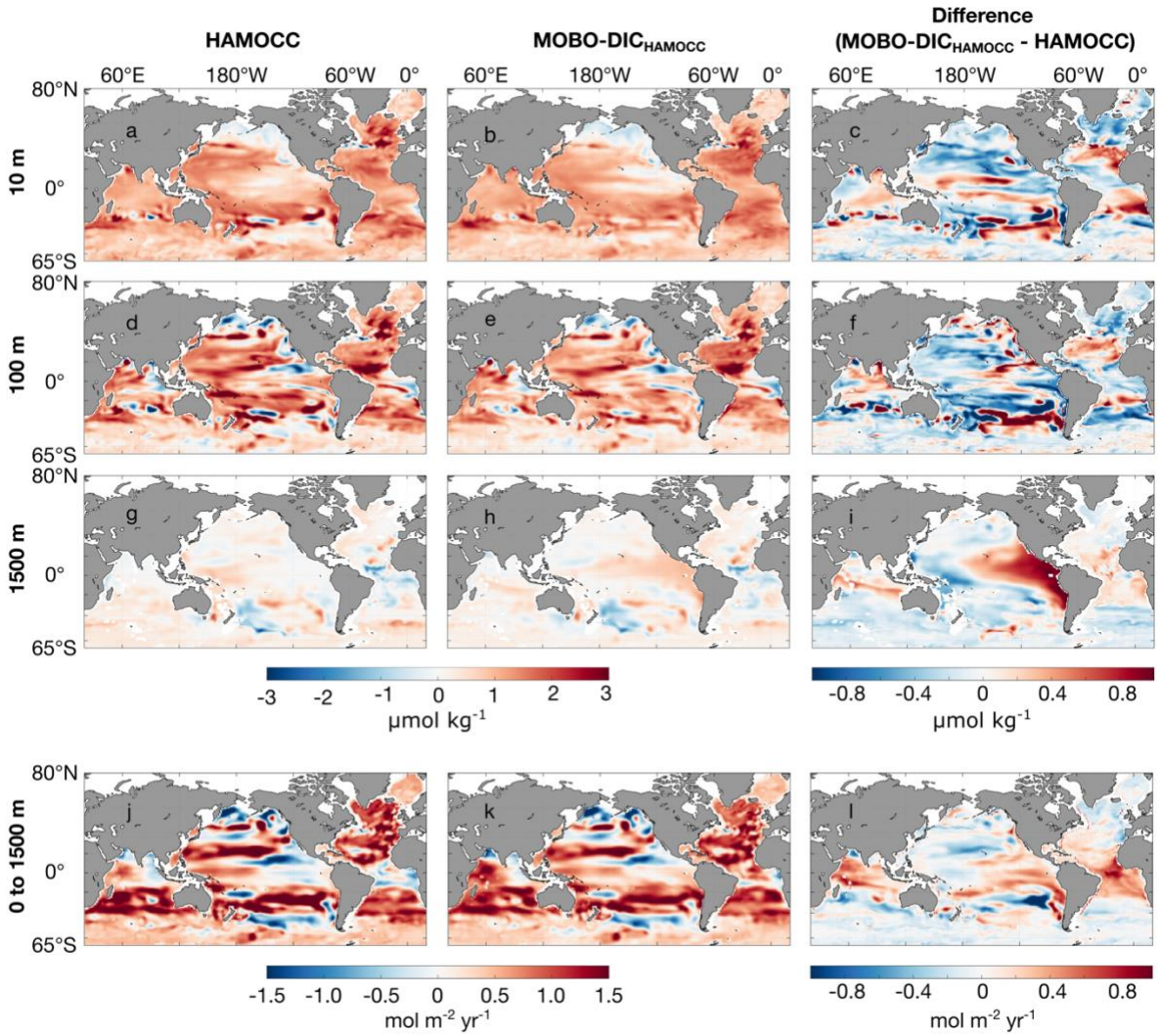

Figure S7: Spatial distribution of the decadal trend of sDIC in HAMOCC (a,d,g), our MOBO-DIC reconstruction of HAMOCC with synthetic data (b,e,h), and the difference between the two (c,f,i) at 10 m (a-c), 100 m (d-f), and vertically integrated decadal trend in the upper 1500 m (g-i).

Our MOBO-DIC method run with synthetic data also captures the patterns and magnitude of the interannual variability of sDIC in HAMOCC well (Fig. S8). Although in some regions, MOBO-DIC over- or underestimates the variability, there is no systemic bias in one direction. Similar as with the trend, we find an over estimation of the interannual variability in our MOBO-DIC reconstruction of HAMOCC. This appears to be an artifact due to overfitting, that is not found in our reconstructions based on real observations.

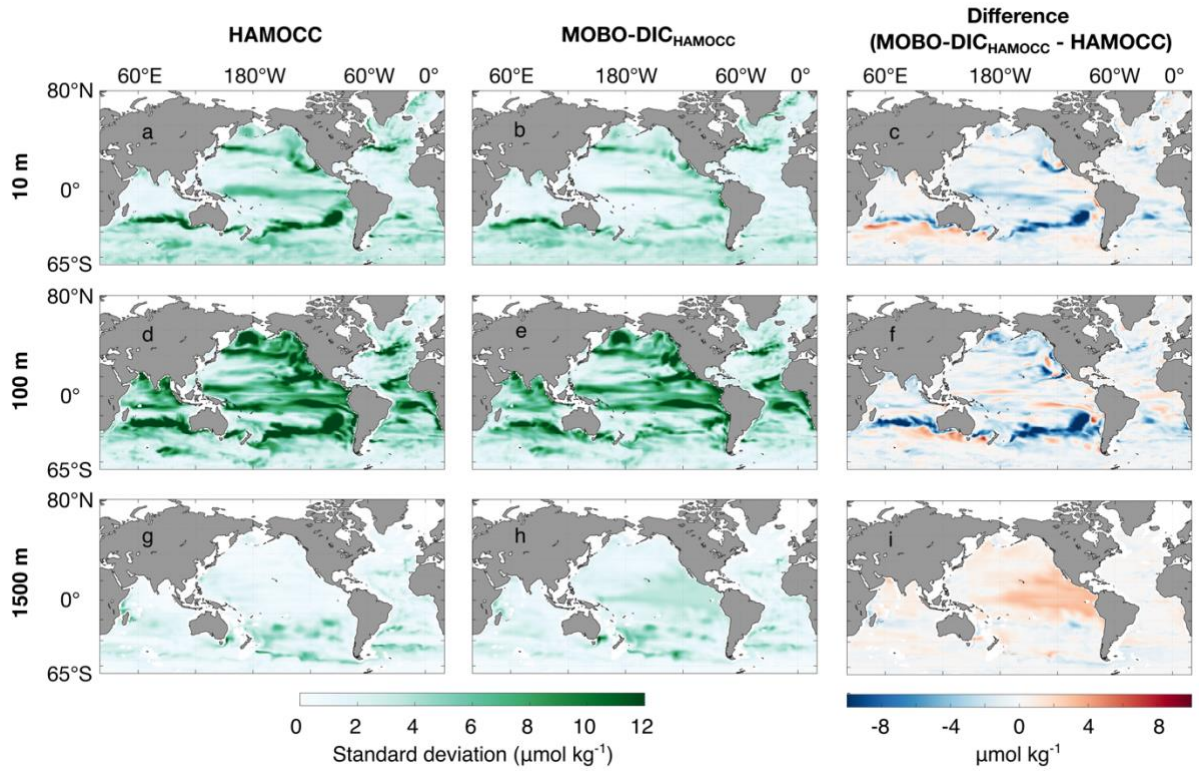

Figure S8: Spatial distribution of the interannual variability of sDIC, defined as the standard deviation in time (de-trended, seasonal cycle smoothed with a 12-month running mean) in HAMOCC (a,d,g), our MOBO-DIC reconstruction of HAMOCC with synthetic data (b,e,h), and the difference between the two (c,f,i) at 10 m (a-c), 100 m (d-f), and 1500 m (g-i).

S6.2 Independent time-series stations (BATS, HOT, Drake Passage)

DIC time-series stations are regularly visited sites, where measurements of DIC are taken. These data are independent from our mapping method, i.e., they are not used to create our data estimate, but provide a crucial basis to estimate how well our estimate compares to measured values. Independent time-series stations that overlap with our study domain and period include the Bermuda Atlantic Time-series Study (BATS; Bates et al., 2014), Hawaii Ocean Time-series (HOT; Dore et al., 2009), and Drake Passage (Munro et al., 2015). See Fig. S1 for the location of these stations.

While the in-situ observations display considerably more noise than our smooth monthly 1°x1° fields, we find that MOBO-DIC is close to the mean values at the time-series stations and captures

some of the variability (Fig. S9). The RMSD between MOBO-DIC and the time-series stations range from 13 µmol kg^{-1} in the shallow waters at HOT to 42 µmol kg^{-1} at the surface of Drake Passage. Some observed values at the time-series stations seem to be outliers and may not be representative of the mean monthly field. For example, the large RMSD at Drake Passage can be at least partially attributed to some very low observed values (~200 µmol kg^{-1} lower than the mean). In addition, MOBO-DIC has a substantial offset in the deeper waters near BATS station, resulting in a large RMSD here too.

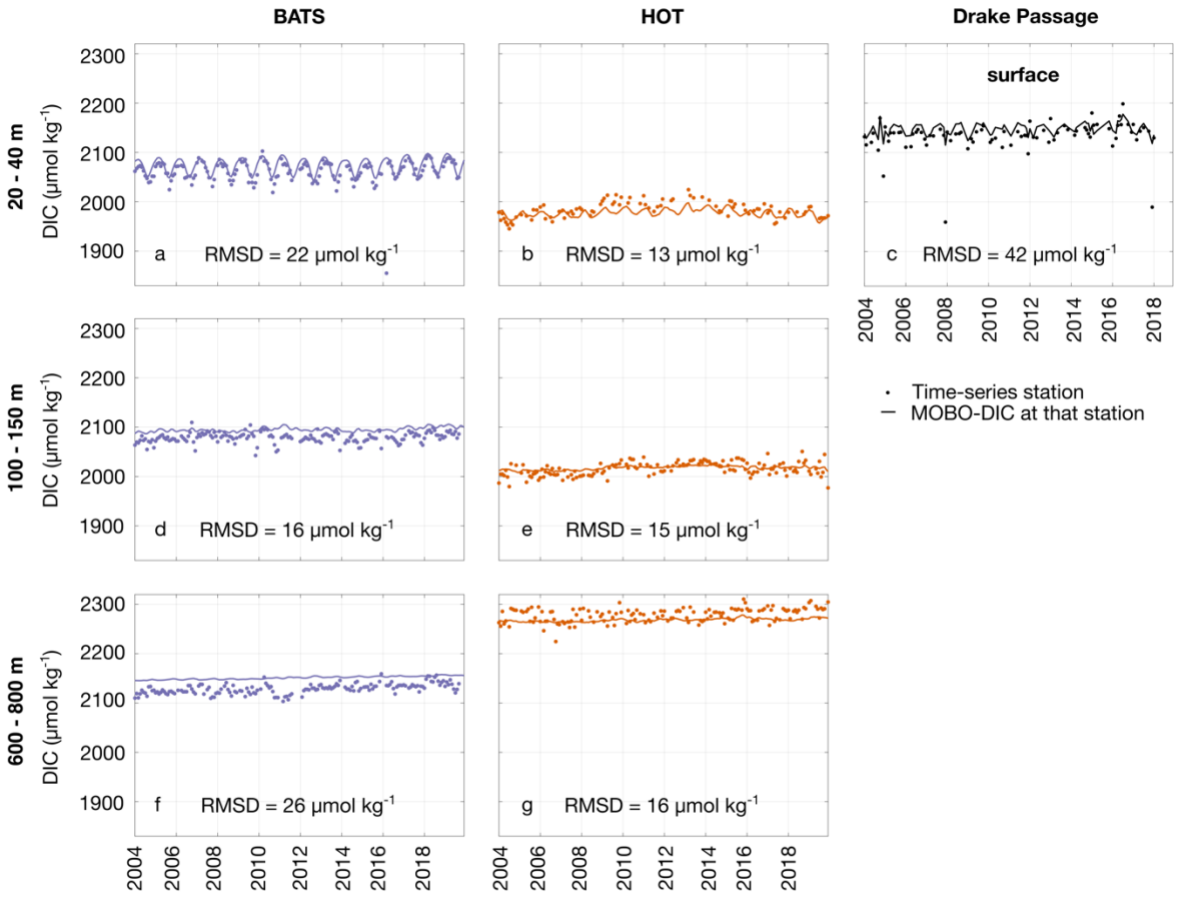

Figure S9: Timeline of DIC between 20 and 40 m (a-c), 100 and 150 m (e-g), and 600 and 800 m (h-j), BATS (a,d,f), HOT (b,e,g), and Drake Passage (surface only, c). Dots illustrate the direct measurements at these stations, solid lines show our MOBO-DIC estimate of DIC at the same month and 1°x1° grid point closest to the sites. RMSD between MOBO-DIC and the time-series stations is shown for each depth range and for each station as text. We chose to display averages over multiple depth levels here as the time-series data is often sparse at individual depth levels.

S6.3 DIC calculated from biogeochemical Argo float measurements (SOCCOM floats)

Argo floats equipped with biogeochemical sensors (BGC Argo floats) have been sampling the global ocean in recent years, supplementing the ship data (https://biogeochemical-argo.org/). They do not measure DIC directly, but several methods have been developed to estimate DIC based on the BGC float measurements of other variables. Some BGC Argo floats are equipped with pH sensors, but these floats are mostly confined to the Southern Ocean as part of the Southern Ocean Carbon and Climate Observations and Modeling project (SOCCOM, https://soccom.princeton.edu/). Here, we make use of DIC calculated based on the temperature, salinity, and pH measurements of the SOCCOM floats, in combination with the LIAR approach to estimate total alkalinity (Carter et al. 2018), and CO2SYS (Humphreys et al., 2020), available at https://soccompu.princeton.edu/www/index.html.

Our comparison with the float data shows that MOBO-DIC captures the variability in the Southern Ocean well (Fig. S10). The discrepancies that exist between MOBO-DIC and the float data can be partially explained by high frequency variability captured by the floats, that are not in our smooth 1°x1° monthly fields. In addition, in the region between the Polar Front (~55°S) and 65°S, our estimate of DIC at the time and location of the floats is substantially less than the DIC estimates by the floats, especially in the winter months (i.e., when the DIC concentrations exhibit the seasonal peak). This finding is in line with previous studies who found that SOCCOM floats report more outgassing (i.e., higher DIC concentrations) in this region in winter than ship-based estimates (Gray et al., 2018; Bushinsky et al., 2019). Notably, this known difference at the surface also exists in the interior (Fig. S10 f,i). However, the difference between the floats and our estimate south of the Polar Front (mean bias of ~8 µmol kg^{-1}) is well within the uncertainty of MOBO-DIC in this region (18 µmol kg^{-1}). Nonetheless, it confirms the known differences between float and ship-based estimates of DIC in this region and further research should be conducted to understand the processes behind that.

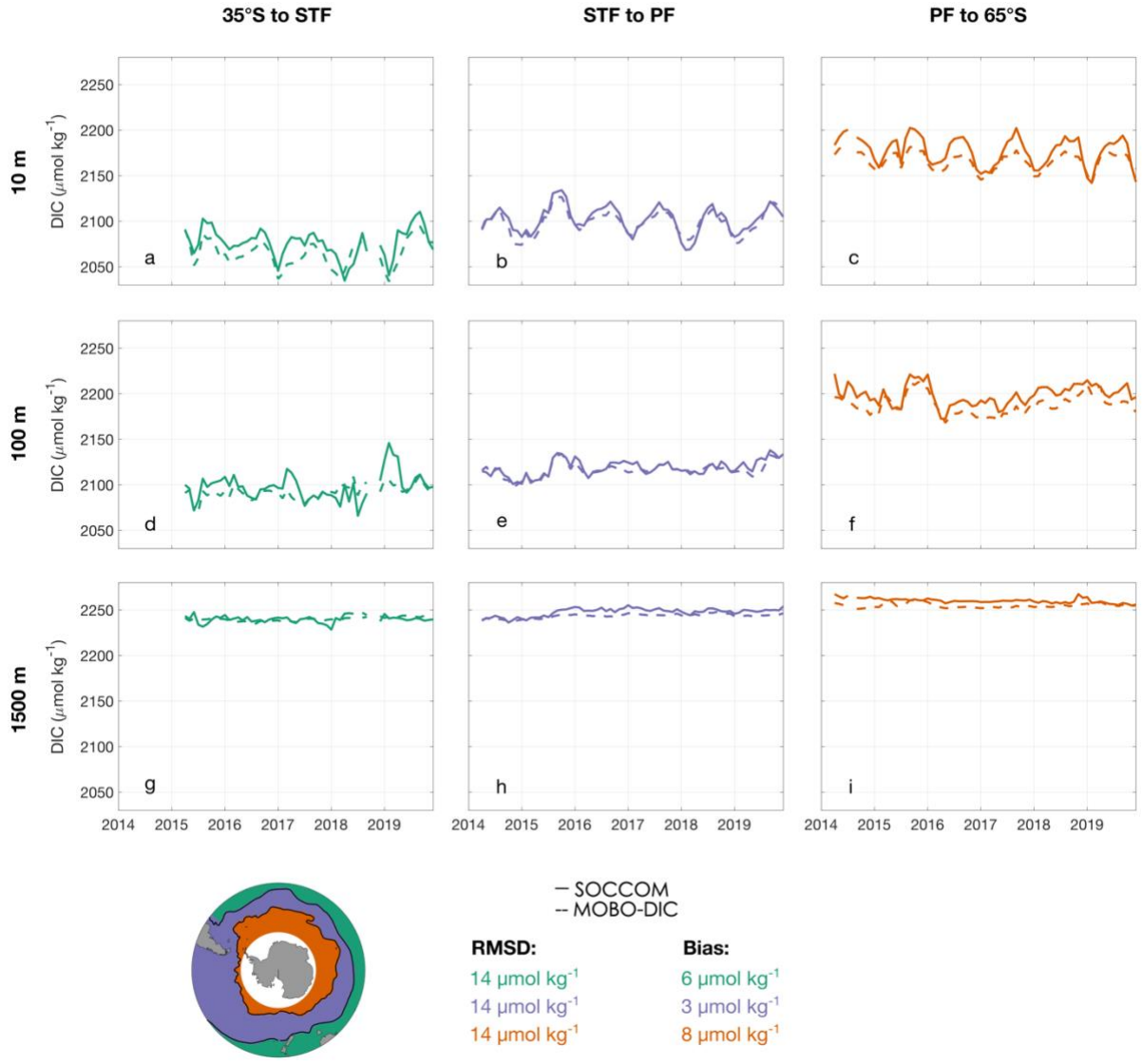

Figure S10: Timeline of mean DIC at 10 m (a-c), 100 m (d-f), and 1500 m (g-i), between 35° S and the Subtropical Front (STF, a,d,g), between the STF and the Polar Front (PF, b,e,h), and between the PF and 65° S (c,f,i). Solid lines illustrate the DIC estimated from the SOCCOM floats, dashed lines show our MOBO-DIC estimate at the same month and 1°x1° grid point closest to each float observation. The panel on the right displays the three interfrontal regions in green, purple, and orange from north to south. The fronts are based on Orsi et al. (1995).

S6.4 Global mapped surface DIC (OceanSODA-ETHZ)

To compare our estimate at a global scale, but restricted to the surface, we compare it to the surface DIC estimate OceanSODA-ETHZ by Gregor & Gruber (2021) at the time and location where the two datasets overlap (January 2004 to December 2018). The approach by Gregor & Gruber (2021) also uses a cluster-regression method with an ensemble of clusters; however, they only estimate surface values. In addition, the DIC in OceanSODA-ETHZ is not based on direct DIC measurements but is calculated based on their cluster-regression estimates of pH and total alkalinity using CO2SYS (Humphreys et al., 2020). Note that for the surface, we consider the shallowest depth level in MOBO-DIC (2.5 m), which is not at the actual surface. We do not normalize for salinity in this comparison, as their estimate uses a different salinity-product than ours.

Considering that the two estimates of DIC are based on independent datasets of measurements (SOCAT vs. GLODAP), their distribution of surface DIC compares well (Fig. S11). Overall, the global mean RMSD between the two data estimates is 15 µmol kg^{-1}, and a global mean bias of 4 µmol kg^{-1} (Fig. S11 a-c). The positive bias cannot be attributed to different periods, as here we only compare the overlap period from 2004 through 2018. A part of this bias could be linked to our shallowest depth being 2.5 m, and not the surface. Both the bias and the RMSD are, however, well within the sum of the uncertainty limits of the two datasets (21 and 18 µmol kg^{-1}, for OceanSODA-ETHZ and MOBO-DIC, respectively).

The trend (Fig. S11 d-f) and interannual variability (Fig. S11 g-i) in the two datasets are also encouragingly similar. The trend of MOBO-DIC at the surface is slightly less in most regions than the trend of the mapped surface DIC from Gregor & Gruber (2021), with global mean trends of 0.6 µmol $kg^{-1}yr^{-1}$ and 0.8 µmol $kg^{-1}yr^{-1}$, respectively (Fig. S11 d-f). The interannual variability of MOBO-DIC at the surface is also slightly smaller in most regions than the interannual variability in OceanSODA-ETHZ Gregor & Gruber (2021), with global mean standard deviations of 3 and 4 µmol kg^{-1}, respectively.

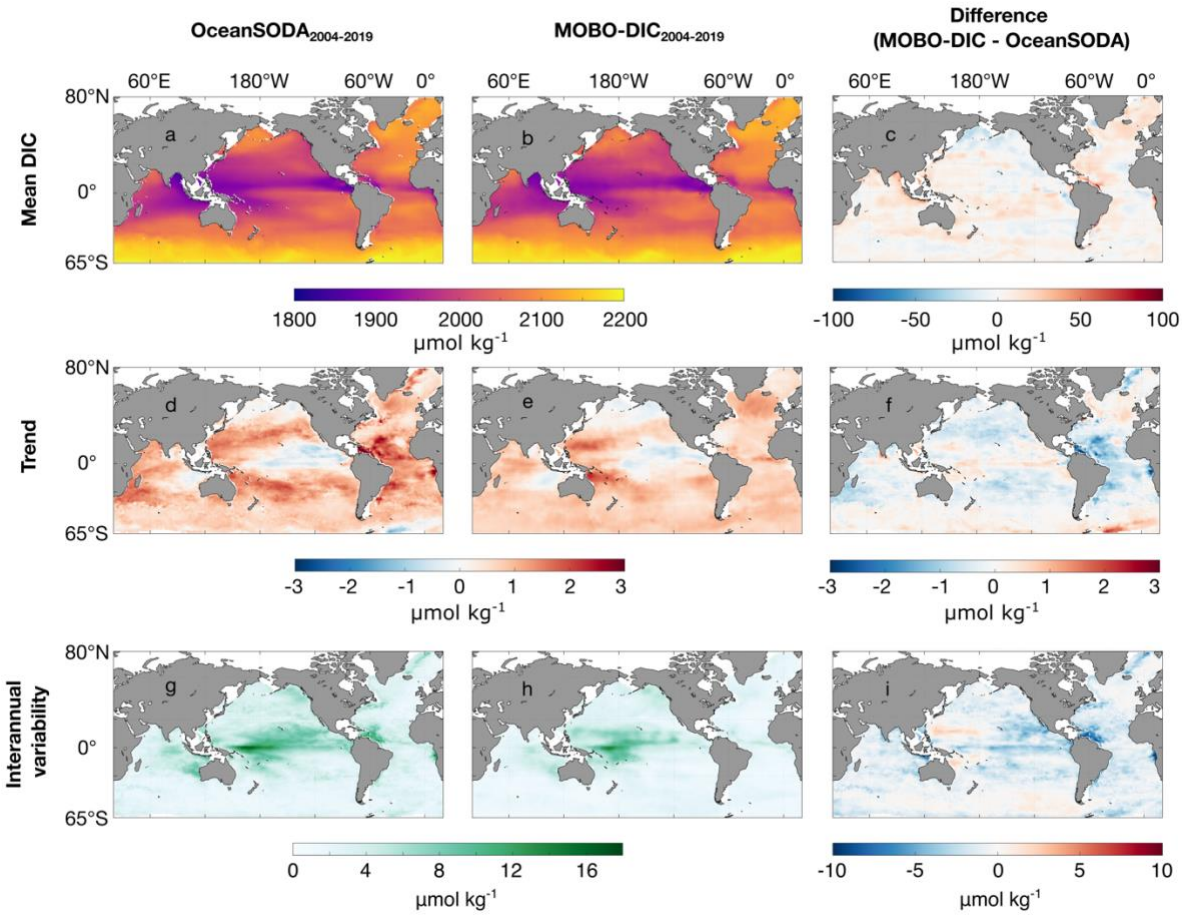

237 **Figure S11:** Mean (a-c), trend (d-f), and interannual variability (g-h) of surface DIC in OceanSODA-ETHZ (a,d,g) and
238 MOBO-DIC at 2.5 m (b,e,h) from January 2004 to December 2018, and the difference between the two estimates
239 (MOBO-DIC - OceanSODA-ETHZ; c,f,i).

240

S7 Trends in sDIC

We illustrate the vertically integrated trend in sDIC in Fig. 2a of the Main Text. Here, we demonstrate the trends on the individual depth levels (Fig. S12). We find that most of the observed negative trends are significant at the 95% confidence intervals, including some negative trends e.g., below the thermocline of the North Pacific.

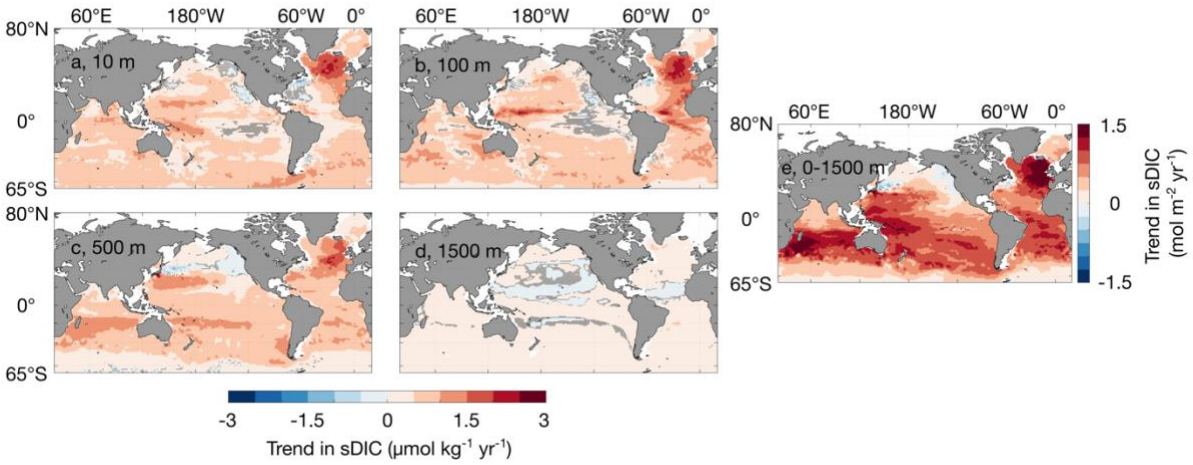

Figure S12: Maps of the trend in sDIC between 2004 and 2020 based on the linear trend at 10 m (a), 100 m (b), 500m (c), 1500 m (d), and vertically integrated over the upper 1500 m (e). In a-d, regions where the trends are not significant ($p<0.05$) are hatched. In e, we remove the trends that are not significant ($p<0.05$) before integrating.

S8 Interannual variability in the Western Equatorial Pacific

We find the largest interannual variations in sDIC below the thermocline in the Western Equatorial Pacific (here: 0.5°N to 14.5°N, 124.5°E to 179.5°E). Here, we compare the connection between the observed variations in sDIC in this region and natural climate variability, represented by the Multivariate El Niño Index (MEI; Wolter et al., 2011). During El Niño periods (positive MEI), the trade winds weaken, leading to less upwelling in the Peruvian Coastal Upwelling System (PCUS), the cold tongue in the eastern equatorial Pacific extends less far towards the west, while the warm pool in the Western Equatorial Pacific retracts eastward (Talley et al., 2011). Thus, overall sea surface temperatures tend to be warmer, and less DIC and nutrients are brought to the surface in the PCUS during El Niño periods. Concurrently, the slope of the thermocline, which has a west-east gradient across the equatorial Pacific flattens, resulting in a shallower mixed layer in the Western Equatorial Pacific. The opposite holds for La Niña periods, i.e., colder SSTs, more sDIC and nutrients in the PCUS, and a steeper slope of the thermocline.

Our results demonstrate a positive correlation between mean sDIC and MEI in the upper Western Equatorial Pacific. This correlation is moderate near the surface ($r = 0.41$ at 10 m), largest around the thermocline ($r = 0.85$ at 150 m) and decreases again below the thermocline ($r = 0.28$ at 500 m, Fig. S13). Temperature cannot be the dominant driver of this signal because the effect of decreased solubility of CO_2 would result in a negative correlation. Instead, the relationship between the sDIC in the water column of the Western Equatorial Pacific and MEI suggests that the shift in the thermocline is the dominant driver for the sDIC variations, in line with model studies from McKinley et al. (2004). The flattening of the thermocline during El Niño periods brings sDIC and nutrients stored at depth upward, explaining the strong positive correlation in the thermocline of this region. This effect diminishes with depth, and above the thermocline, the effect is reduced through outgassing and biological activity as proposed by Takahashi et al. (2002) and subsequent studies (e.g., Feely et al., 2006).

Compared to the signal in the Western Equatorial Pacific, we observe a smaller signal in the PCUS. It seems that here, opposing effects on the sDIC mostly cancel each other out, resulting in the

279 weak interannual variability of sDIC in this region. Here, decreased upwelling during El Niño
280 periods leads to less DIC being brought to the surface. Concurrently, less upwelled nutrients result
281 in less biological uptake of DIC, and thus, more DIC remaining near the surface.
282
283 Our findings are consistent with the findings by McKinley et al. (2004), who used a global ocean
284 general circulation model to link their model's variability of the air-sea CO_2 fluxes in the equatorial
285 Pacific to ENSO-induced changes in the transport of DIC: the combined effects of the flattening of
286 the thermocline, less upwelling, and the east-west displacement of the warm pool change how
287 much DIC-rich water reaches the surface and affects the air-sea CO_2 fluxes. However, that study
288 finds large variabilities across most longitudes of the equatorial Pacific, with the largest variations
289 near the center and the east, compared to our study, where the largest variations are in the
290 Western Equatorial Pacific. This may be linked to the recent westward shift of the El Niño
291 phenomena also referred to as El Niño Modoki (Ashok et al., 2007).

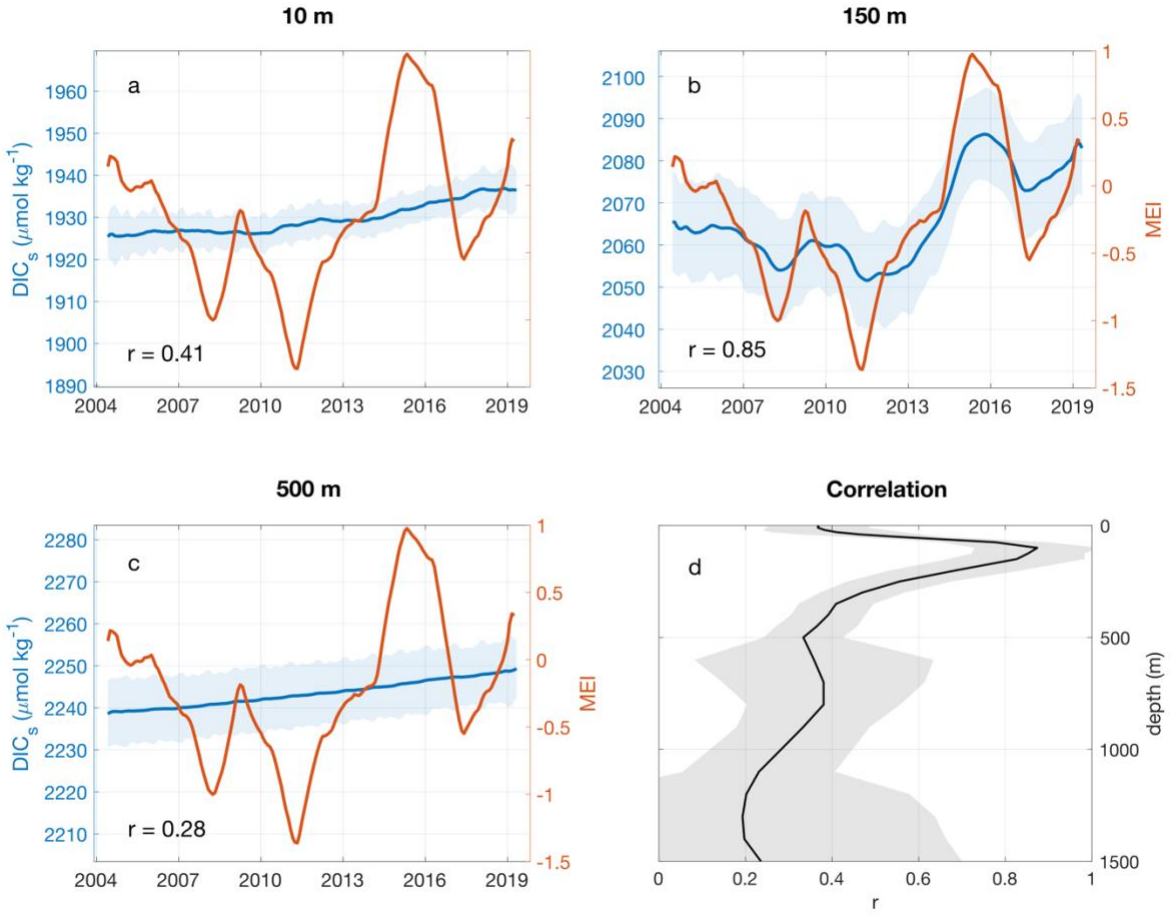

Figure S13: ENSO and sDIC in the Western Equatorial Pacific. Timelines of the mean sDIC in the western equatorial Pacific (left y-axis, blue) and the MEI (right y-axis, orange) at 10 m (a), 150 m (b), and 500 m (c) both sDIC and the MEI are smoothed with a 12-month moving average. The first and last 6 months are lost in the smoothing. The blue shading indicates the ensemble spread, i.e., the prediction uncertainty. Correlation coefficient r between sDIC in this region (seasonal cycle removed) and the MEI (seasonal cycle removed) as a function of depth (d). The correlation coefficient r between sDIC and the MEI is shown as text for each depth level in a-c.